Origin of the mass splitting of azimuthal anisotropies in a multiphase transport model

Hanlin Li,[1,2] Liang He,[2] Zi-Wei Lin,[3,4] Denes Molnar,[2] Fuqiang Wang,[5,2,*] and Wei Xie[2]

[1]*College of Science, Wuhan University of Science and Technology, Wuhan, Hubei 430065, China*

[2]*Department of Physics and Astronomy, Purdue University, West Lafayette, Indiana 47907, USA*

[3]*Department of Physics, East Carolina University, Greenville, North Carolina 27858, USA*

[4]*Key Laboratory of Quarks and Lepton Physics (MOE) and Institute of Particle Physics, Central China Normal University, Wuhan, Hubei 430079, China*

[5]*School of Science, Huzhou University, Huzhou, Zhejiang 313000, China*

Both hydrodynamics-based models and a multiphase transport (AMPT) model can reproduce the mass splitting of azimuthal anisotropy (v_n) at low transverse momentum ($p_\perp$) as observed in heavy ion collisions. In the AMPT model, however, v_n is mainly generated by the parton escape mechanism, not by the hydrodynamic flow. In this study we provide detailed results on the mass splitting of v_n in this transport model, including v_2 and v_3 of various hadron species in d+Au and Au+Au collisions at the Relativistic Heavy Ion Collider and p+Pb collisions at the Large Hadron Collider. We show that the mass splitting of hadron v_2 and v_3 in AMPT first arises from the kinematics in the quark coalescence hadronization process, and then, more dominantly, comes from hadronic rescatterings, even though the contribution from the latter to the overall charged hadron v_n is small. We further show that there is no qualitative difference between heavy ion collisions and small-system collisions or between elliptic (v_2) and triangular (v_3) anisotropies. Our studies thus demonstrate that the mass splitting of v_2 and v_3 at low $p_\perp$ is not a unique signature of hydrodynamic collective flow but can be the interplay of several physics effects.

I. INTRODUCTION

The quark-gluon plasma was created in relativistic heavy ion collisions, and extensive efforts are going on to study quantum chromodynamics at the extreme conditions of high temperature and energy density [1–5]. Of particular interest are noncentral heavy ion collisions, where the overlap volume of the colliding nuclei is anisotropic in the transverse plane perpendicular to the beam direction. One interesting finding is that the collision system is explosive, consistent with the buildup and expansion of the hydrodynamic pressure [6–8]. The pressure gradient and/or particle interactions would generate an anisotropic expansion, which converts the anisotropic geometry into the final-state elliptic flow [9]. In addition, because of fluctuations in the initial-state collision geometry, there is an elliptic harmonic anisotropy in the configuration space (ϵ_2) even in central heavy ion or proton-nucleus collisions [10]. Furthermore, fluctuations lead to finite configuration space harmonics of all orders [11], which will result in final-state momentum anisotropies of all orders (v_n), where n is a positive integer.

The mass splitting of hadron v_2 at low transverse momentum ($p_\perp$) is also observed in the experimental data. It is often considered as a hallmark of the hydrodynamic description of relativistic heavy ion collisions [6], where a common but anisotropic transverse velocity field coupled with the Cooper-Frye hadronization mechanism [12] leads to the mass splitting. Furthermore, results from hybrid models, where hydrodynamics is followed by a hadron cascade, have shown

that the v_2 mass splitting is small just after hadronization and is then strongly enhanced by hadronic scatterings [13–15].

Large v_n values have been observed in large-system heavy ion collisions, and both hydrodynamics-based models [6–8] and a multiphase transport (AMPT) model [16–18] can reproduce these results. Later particle correlation data in small systems, including d+Au [19,20] collisions at the Relativistic Heavy Ion Collider (RHIC) and high multiplicity p+p [21] or p+Pb [22–24] collisions at the Large Hadron Collider (LHC), hint at similar v_n (and mass splitting). Again, both hydrodynamics [25,26] and a multiphase transport [27] can reasonably describe the experimental data. This seems puzzling, because naively one would expect the small system to be far from equilibrium and thus not suitable for a hydrodynamical description.

A recent study by some of us [28,29] using AMPT has shown that the azimuthal anisotropy is mainly generated by the anisotropic parton escape and that hydrodynamics may play only a minor role. This escape mechanism would naturally explain the similar azimuthal anisotropies in heavy ion and small system collisions. Because mass splitting of hadron v_2 is also present in the AMPT results, it suggests that the hydrodynamic collective flow may not be the only mechanism that can generate the mass splitting of hadron v_n in collisions with high energy densities.

In an earlier study [30] we used AMPT simulations of Au+Au and d+Au collisions at the top RHIC energy to investigate the mass splitting of v_2 of pions, kaons, and protons. We found that the mass splitting of v_2 in AMPT is partly from the kinematics in the quark coalescence process but mainly from hadronic rescatterings [30]. In this paper we expand that study to more hadron species including ρ, K^*, ϕ, Δ,

*fqwang@purdue.edu

and strange hadrons such as Λ and Ξ. We also investigate the massing splitting of the triangular flow v_3 and include AMPT results of $p+$Pb collisions at the LHC energy of 5 TeV. In addition, we provide details of our analysis, such as the effect of the finite opening angles among coalescing partons, the difference between primordial hadrons and hadrons from resonance decays, and the connection between the v_2 mass splitting and the initial hadron spatial eccentricity.

II. MODEL AND ANALYSIS

We employ the same version of the string melting AMPT model (v2.26t5, available online at [31]) as in earlier studies [28–30]. It consists of a fluctuating initial condition, parton elastic scatterings, quark coalescence for hadronization, and hadronic interactions. The initial energy and particle productions are being described by the HIJING model. However, the string melting AMPT model converts these initial hadrons to their valence quarks and antiquarks, based on the assumption that the high energy density in the overlap region of high energy heavy ion collisions requires us to use parton degrees of freedom to describe the dense matter [16]. Two-body elastic parton scatterings are treated with Zhang's parton cascade (ZPC) [32], where we take the strong coupling constant $\alpha_s = 0.33$ and a total parton scattering cross section $\sigma = 3$ mb for all AMPT calculations in this study. After partons stop interacting, a simple quark coalescence model is applied to describe the hadronization process that converts partons into hadrons [17]. Subsequent interactions of these formed hadrons are modeled by a hadron cascade [17].

Two of the above components, the hadronization process and hadron cascade, are especially relevant for this study. Hadronization in the string melting version of AMPT is modeled with a simple quark coalescence, where two nearest partons in space (one quark and one antiquark) are combined into a meson and three nearest quarks (or antiquarks) are combined into a baryon (or antibaryon). In addition, when the flavor composition of the coalescing quark and antiquark allows the formation of either a pseudoscalar or a vector meson, the meson species whose mass is closer to the invariant mass of the coalescing parton pair will be formed. The same criterion is also applied to the formation of an octet or a decuplet baryon with the same flavor composition. Thus in these situations the hadron species that has a larger mass will be typically formed when the coalescing partons have a larger invariant mass.

The hadron cascade in the AMPT model includes explicit particles such as π, ρ, ω, η, K, K^*, ϕ mesons, N, Δ, $N^*(1440)$, $N^*(1535)$, Λ, Σ, Ξ, Ω, and deuteron and the corresponding antiparticles [33]. Hadronic interactions include meson-meson, meson-baryon, and baryon-baryon elastic and inelastic scatterings. For example, meson-baryon scatterings includes pion-nucleon, ρ-nucleon, and kaon-nucleon elastic and inelastic processes, among many reaction channels. More details can be found in the main AMPT paper [17]. We terminate the hadronic interactions at a cutoff time (t_{max}), when the observables of interest are stable; a default cutoff time of $t_{max} = 30$ fm/c is used here.

In this study we simulate three collision systems: Au+Au collisions at RHIC with $b = 6.6$–8.1 fm (corresponding to

approximately 20%–30% centrality [8]) at the nucleon-nucleon center-of-mass energy $\sqrt{s_{NN}} = 200$ GeV, $d+$Au collisions at RHIC with $b = 0$ fm at $\sqrt{s_{NN}} = 200$ GeV, and $p+$Pb collisions at LHC with $b = 0$ fm at $\sqrt{s_{NN}} = 5$ TeV. Note that the string melting version of AMPT can reasonably reproduce the particle yields, $p_\perp$ spectra, and v_2 of low-$p_\perp$ pions and kaons in central and mid-central Au+Au collisions at 200A GeV and Pb+Pb collisions at 2760A GeV [18].

The initial geometric anisotropy of the transverse overlap region of a heavy ion collision is often described by the eccentricity of the nth harmonic order [11]:

$$\epsilon_n = \sqrt{\langle r_\perp^2 \cos n\phi_r \rangle^2 + \langle r_\perp^2 \sin n\phi_r \rangle^2}/\langle r_\perp^2 \rangle. \qquad (1)$$

Here $r_\perp$ and ϕ_r are the polar coordinate of each initial parton (after its formation time) in the transverse plane, and $\langle ... \rangle$ denotes the per-event average. We follow the same method as in our earlier studies [28,30] to calculate azimuthal anisotropies. In particular, we compute the nth harmonic plane (short-axis direction of the corresponding harmonic component) of each event from its initial configuration of all partons [34] according to

$$\psi_n^{(r)} = \frac{1}{n}[\text{atan2}(\langle r_\perp^2 \sin n\phi_r \rangle, \langle r_\perp^2 \cos n\phi_r \rangle) + \pi]. \qquad (2)$$

The momentum anisotropies are then characterized by Fourier coefficients [35],

$$v_n^{\text{obs}} = \langle \cos n(\phi - \psi_n^{(r)}) \rangle, \qquad (3)$$

where ϕ is the azimuthal angle of the parton or hadron momentum. Note that all results shown in this paper are for particles (partons or hadrons) within the pseudorapidity window of $|\eta| < 1$.

III. PARTONIC ANISOTROPY

Currently the string melting version of the AMPT model [16,17,31] has only quarks but no gluons, where the gluon degree of freedom can be considered as being absorbed in the quark's. Note that the scattering cross sections in the parton cascade are set to be the same regardless of quark flavors. Figure 1 shows the v_2 and v_3 of the u and d light quarks and the s strange quarks in three systems: Au+Au and $d+$Au collisions at 200 GeV, and $p+$Pb collisions at 5 TeV. The quark and antiquark anisotropies are found to be the same, so they are combined. There is practically no difference between the u and d quark v_n's, so they are also combined in Fig. 1. The v_n magnitudes are similar among the three systems, except v_3 in $d+$Au which is significantly lower than the other two systems. In general small systems should generate lower v_n than large systems, and this is the case for v_3 between $d+$Au and Au+Au collisions. The v_2 in $d+$Au is not much smaller than that in Au+Au, possibly because the lower energy density in $d+$Au is compensated by the larger elliptical eccentricity (ϵ_2). The v_n in $p+$Pb are not much smaller than those in Au+Au, and this may be because the smaller system size is compensated by the larger collision energy.

At low $p_\perp$ the light quark v_2 is larger than the s quark's. This is qualitatively consistent with the hydrodynamic picture where particles move with a common collective flow velocity.
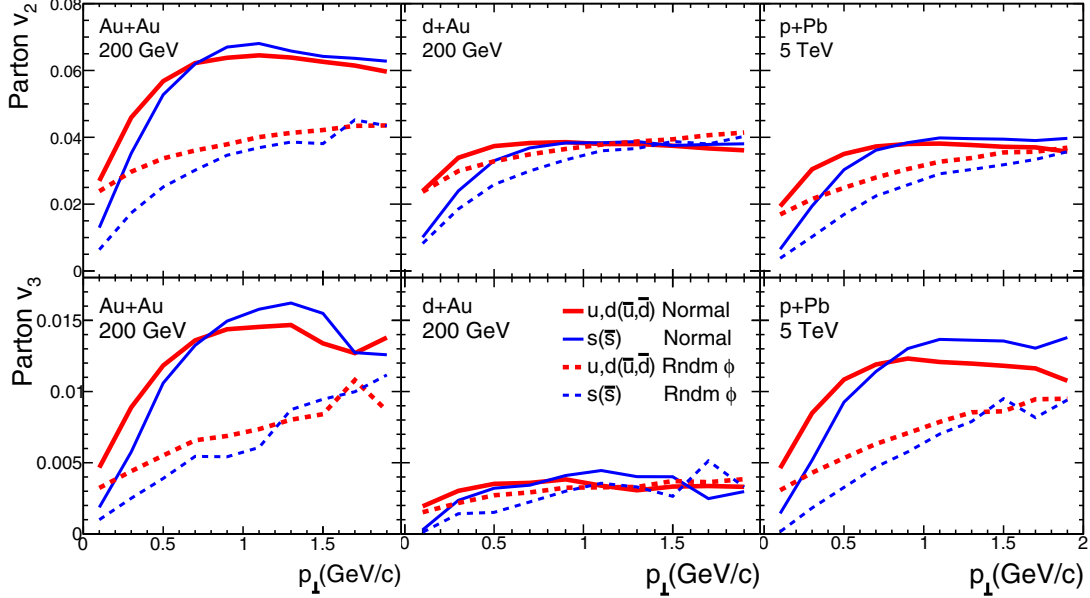
FIG. 1. Parton v_n. Parton v_2 (top panels) and v_3 (bottom panels) as a function of $p_\perp$ for light (u and d) and strange (s) (anti-)quarks in the final state before hadronization from AMPT with string melting. Three systems are shown: $b = 6.6-8.1$ fm Au+Au collisions at $\sqrt{s_{\mathrm{NN}}} = 200$ GeV (left column), $b = 0$ fm d+Au collisions at 200 GeV (middle column), and $b = 0$ fm p+Pb at 5 TeV (right column). Both normal (solid curves) and ϕ-randomized (dashed curves) AMPT results are shown, with thick curves for light quarks and thin curves for strange quarks.

Because particles have the same v_n at the same speed, $v_n(p_\perp)$ as a function of $p_\perp$ are split according to particle masses. This mass splitting between light and strange quarks is observed in both v_2 and v_3 and in all three systems.

Because our previous studies [28,29] have shown that v_2 comes largely from the anisotropic escape mechanism, then the question is whether or not the observed mass splitting is entirely from the minor contributions from hydrodynamics. So we also carry out a test calculation with no collective anisotropic flow by randomizing the outgoing parton azimuthal directions after each parton-parton scattering as in Ref. [28]. The results are shown by the dashed curves in Fig. 1, where the differences between the light quark and strange quark v_n's are still present. Because the parton azimuthal angles are now randomized, the final-state parton anisotropy is entirely from the anisotropic escape mechanism [28]. The fact that the mass splitting is similar between the normal and ϕ-randomized AMPT suggests that it is caused by the mass or kinematic difference in the scatterings rather than the collective flow. At high $p_\perp$ the light quark and strange quark v_n's approach each other; this is expected because the mass difference becomes unimportant at high $p_\perp$.

IV. MASS SPLITTING FROM QUARK COALESCENCE

Because there is mass splitting in the quark v_n, it is natural to expect mass splitting in the v_n of hadrons with different quark contents. However, for hadrons such as pions, ρ mesons, and protons made of light quarks only, the difference between their anisotropies must come from the hadronization process and/or hadronic rescatterings. We first study the effect of the former by examining v_2 of hadrons right after hadronization but before

hadron rescatterings take place. Figure 2 shows the v_2 and v_3 of primordial π, K, ϕ, $p(\bar{p})$, $\Lambda(\bar{\Lambda})$, $\Xi(\bar{\Xi})$ as a function of $p_\perp$ in the three systems we studied. Note that primordial hadrons are hadrons formed directly from hadronization but before resonance decays and hadronic scatterings. In Au+Au collisions the particle v_n exhibit the familiar mass ordering at low $p_\perp$: The v_n's of pions are larger than those of kaons which are in turn larger than those of (anti-)protons and strange baryons. The mass splittings in the small systems of d+Au and p+Pb are not necessarily the same ordering as in the Au+Au system. In this section we study how this mass splitting comes about. We will concentrate on v_2 but the discussions can be extended to v_3.

Because the string melting version of AMPT forms hadrons via quark coalescence, the difference in the pion and proton v_2 comes from the difference in the number of constituent quarks and in the kinematics of those quarks. At high $p_\perp$ the hadron v_2 was measured to exhibit the number of constituent quark (NCQ) scaling:

$$v_2^{\mathrm{B}}/3 \approx v_2^{\mathrm{M}}/2, \qquad (4)$$

where the superscript "B" stands for baryons and superscript "M" for mesons. This comes naturally from quark coalescence, where two or three relatively high $p_\perp$ quarks are almost collimated and coalesce into a meson or baryon. The meson and baryon take on twice and three times the quark v_2 (which are saturated at high $p_\perp$ as in Fig. 1), respectively. This NCQ scaling is evident in Fig. 2; the baryons in each graph approach a similar magnitude of v_n in the higher $p_\perp$ region.

However, this quark collimation picture cannot be extended to low $p_\perp$, because there the relative momentum among constituent quarks could be comparable to the hadron $p_\perp$,
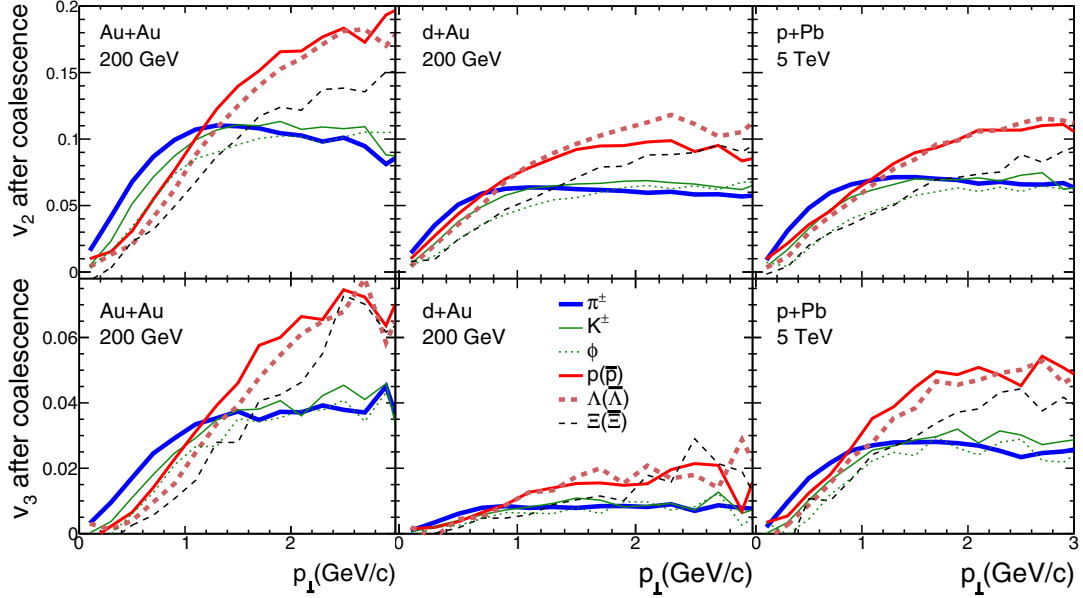
FIG. 2. Mass splitting from coalescence. Primordial hadron v_2 (top panels) and v_3 (bottom panels) as a function of $p_\perp$ right after quark coalescence but before hadronic rescatterings take place in AMPT with string melting. Three systems are shown: $b = 6.6-8.1$ fm Au+Au collisions at $\sqrt{s_{NN}} = 200$ GeV (left column), $b = 0$ fm d+Au collisions at 200 GeV (middle column), and $b = 0$ fm p+Pb at 5 TeV (right column). Thick solid curves are for charged pions, thin solid curves for charged kaons, thin dashed curves for ϕ mesons, medium thick solid curves for (anti-)protons, thick dashed curves for $\Lambda(\bar{\Lambda})$, and medium thick dashed curves for $\Xi(\bar{\Xi})$.

i.e., there will be finite opening angles among the constituent quarks. Therefore the kinematics in the coalescence process [36] such as finite opening angles could lead to the mass splitting of v_2 at low $p_\perp$. To quantitatively understand this, we show in Fig. 3(a) the $p_\perp$ distributions for partons coalescing into pions and protons of $p_\perp = 1$ GeV/c. We have also depicted in the plots the ρ meson, which has the same constituent quark content as the π but a larger mass. Figure 3(b) shows the absolute difference between the azimuthal angle of the constituent quark and that of the formed hadron, $\Delta\phi = |\phi_q - \phi_h|$. Because of the finite angles, the average $p_\perp$ of the constituent quarks is larger than one-half (one-third) of the pion (proton) $p_\perp$. While the actual kinematics are complex, one may verify that a pair (or triplet) of partons with an average transverse momentum $p_\perp^q$ at the average opening angle (as in Fig. 3) gives the composite hadron $p_\perp^h$ roughly as

$$p_\perp^h \approx n_q p_\perp^q \cos(\Delta\phi), \tag{5}$$

where the superscripts "h" and "q" stand for hadrons and constituent quarks, respectively, and n_q is the number of constituent quarks for the given hadron type.

Similarly, because of the finite opening angle the hadron v_2 is not simply twice (or three times) the average quark v_2 at the corresponding average quark $p_\perp^q$. This is shown in Fig. 4, where the quark v_2 is plotted at the $p_\perp$ of the hadron it coalesces into, together with the hadron v_2 from Fig. 2. Note that the quark v_2 in Fig. 1 includes all quarks (i.e., from all hadrons) while that in Fig. 4 is categorized by the formed hadrons. As seen from Fig. 4, the hadron v_2's shown in solid curves are smaller than twice (three times) the quarks shown in dashed curves. Note that the shapes of the quark v_2 curves are different from each other because they are plotted at the

hadron $p_\perp$ and because $p_\perp$ samplings of quarks into pions, ρ mesons, and protons are different (c.f. Fig. 3). One may get a semiquantitative understanding of the hadron $v_2(p_\perp)$ curve by, again, using the average quark kinematics. The hadron azimuthal distribution is

$$\Pi_{i=1}^{n_q}\left[1 + 2v_2^q \cos(2\phi_{q,i})\right] \approx 1 + 2n_q v_2^q \cos(2\Delta\phi)\cos(2\phi_h). \tag{6}$$

Thus the hadron v_2 is given by

$$v_2^h(p_\perp^h) = n_q v_2^q(p_\perp^q)\cos(2\Delta\phi). \tag{7}$$

One may verify that this relationship, with the kinematics in Fig. 3, can approximately describe the v_2 relationship between a hadron at $p_\perp = 1$ GeV/c and its constituent quarks in Fig. 4.

Although v_2 is largely from the escape mechanism, there does exist a contribution from hydrodynamics in AMPT [28,29]. Thus we also carry out the test calculations with no collective anisotropic flow by randomizing the outgoing parton azimuthal directions after each parton-parton scattering as in Refs. [28,29]. The results are shown in Fig. 4 (bottom). In the ϕ-randomized case, the final-state freezeout anisotropy is entirely from the anisotropic escape mechanism. Because mass splitting is also observed in the randomized case, it indicates that the hydrodynamical collective flow is not required to generate the mass splitting in v_n right after hadronization.

V. EFFECTS OF RESONANCE DECAYS

What are shown in Fig. 4 are the v_2 values of primordial hadrons (obtained right after the quark coalescence in the AMPT evolution), not those of hadrons after resonance decays. Figure 5 shows the fraction of primordial pions, kaons, and protons as a function of $p_\perp$. Because what we measure in
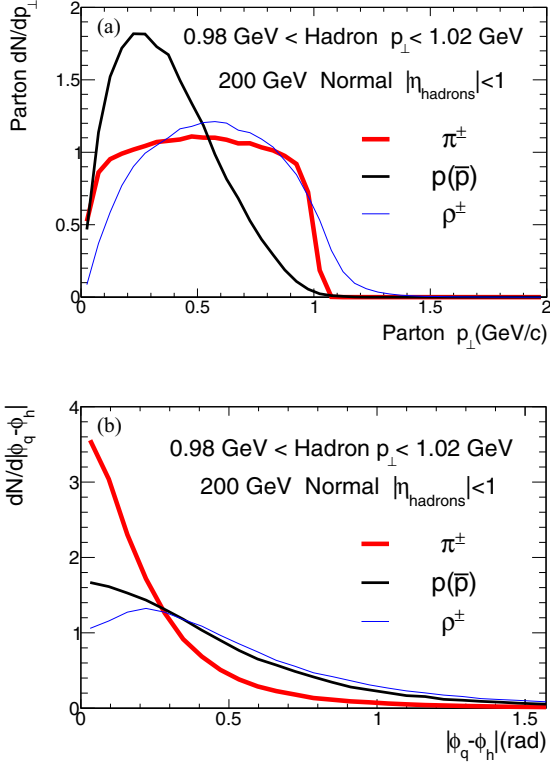
FIG. 3. Coalescence kinematics. Final-state $p_\perp$ (a) and azimuthal opening angle (b) distributions of constituent (anti-)quarks forming π, ρ, and (anti-)proton. Shown are string melting AMPT results for $b = 6.6-8.1$ fm Au+Au collisions at 200 GeV.
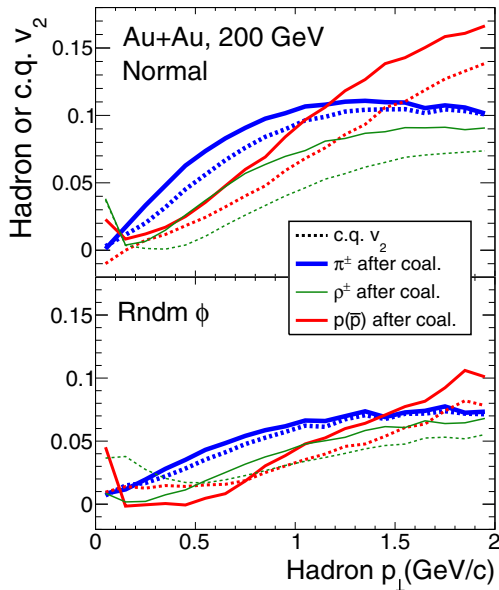

FIG. 4. Conversion of constituent quark v_2 into hadron v_2 by coalescence. Primordial hadron and constituent quark v_2, both plotted as a function of the *hadron* $p_\perp$. The hadron v_2 is taken before any hadronic rescatterings and the constituent quark v_2 is taken just before coalescence. Shown are both normal (top) and ϕ-randomized (bottom) string melting AMPT results for $b = 6.6-8.1$ fm Au+Au collisions at 200 GeV.

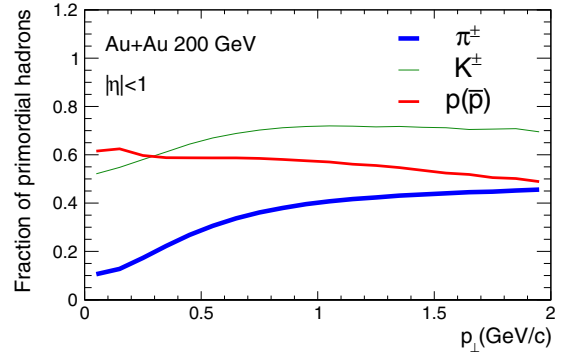

FIG. 5. Decay contributions. Fraction of primordial hadrons in $b = 6.6-8.1$ fm Au+Au collisions at 200 GeV from string melting AMPT where hadronic rescatterings are turned off.

detectors are particles after strong decays, we need to include the effects of resonance decays on v_n. In this section, we thus set the maximum hadronic stage to $t_{\max} = 0.6$ fm/c in AMPT (parameter NTMAX=3) which turns off hadronic rescatterings. We then obtain the final-state hadron v_n that include decays. Note that the final freezeout particles in AMPT include all strong decays of resonances but no electromagnetic or weak decays by default (except for the Σ^0 decay to include its feed down to Λ) [17].

Figure 6 (left) shows the v_2 of primordial pions, primordial ρ's, pions from ρ decays, and all pions. The middle panel shows the corresponding results for kaons where the K^* decay channel is studied. The right panel shows the v_2 of primordial (anti-)protons, primordial (anti-)Δ^0's (as an example), protons from (anti-)Δ^0 decays (as an example), and all protons. We see that at low $p_\perp$ heavier primordial particles have smaller v_2. In addition, the decay product v_2 is usually smaller than their parent v_2. As a result, the v_2's of final-state hadrons including the decay products are smaller than (or closely follow) those of the primordial particles. This reduction effect is stronger in pions than protons, because a bigger fraction of pions comes from resonance decays than protons according to Fig. 5 and because the protons retain more of the parent v_2 than pions from kinematics.

Our results generally agree with those in Refs. [37–39]. It is interesting to note that the ρ-decay pion v_2 curve at low $p_\perp$ does not follow the trend of the parent ρ-meson v_2. Because the decay pion momentum in the ρ rest frame is about 0.36 GeV/c, to have a low-$p_\perp$ daughter pion in the laboratory frame, the ρ decay must be very asymmetric: one pion at low $p_\perp$ and the other at high $p_\perp$. The high-$p_\perp$ pion closely follows the parent ρ direction, while the low-$p_\perp$ pion aligns more perpendicularly because of momentum conservation. With positive v_2 of the ρ, there are therefore relatively more low-$p_\perp$ decay pions perpendicular to the reaction plane, hence a negative pion v_2. We have verified that this feature is also true for the pions from Δ decays.

Figure 7 shows the hadron v_2 and v_3 as a function of $p_\perp$ including contributions from resonance decays. The reduction in v_n is evident in Fig. 7 in comparison with Fig. 2 where only the primordial hadron v_n's are shown. Because of the larger reduction in pion v_n than in proton v_n because of decays, the
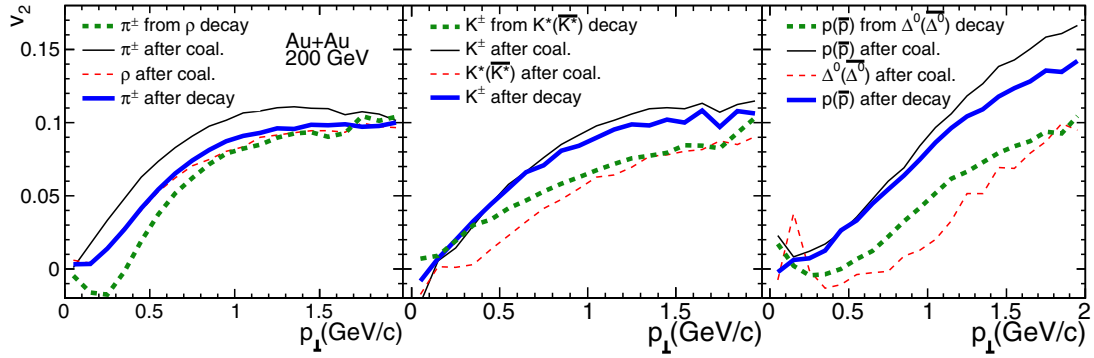
FIG. 6. Effect of decays on v_2. The v_2 of primordial hadrons (thin solid curves), resonances (thin dashed curves), decay products (thick dashed curves), and the total v_2 including both the primordial hadrons and decay products (thick solid curves). Shown are $b = 6.6-8.1$ fm Au+Au collisions at 200 GeV from string melting AMPT where hadronic scatterings are turned off.

amount of mass splitting is reduced. Depending on the magnitude of this reduction, the mass splitting between primordial hadrons right after coalescence may or may not survive once including the decay products. So in general the mass splitting effect decreases after including the decay products.

VI. MASS SPLITTING FROM HADRONIC RESCATTERINGS

Another source of mass splitting of v_n comes from hadronic rescatterings. In the following we study v_n as a function of the degree of hadronic rescatterings. We achieve this by varying the maximum allowed time t_{max} of the hadronic interaction stage in AMPT. So t_{max} can be considered as a qualitative

indicator of the amount of hadronic rescatterings. Note that there is no cutoff time for the partonic evolution in AMPT.

Figure 8 (top panels) shows the v_2 of charged pions, charged kaons, (anti)protons, and charged hadrons (here defined as the sum of charged pions, kaons, protons, and antiprotons) at freezeout in mid-central Au+Au collisions versus $p_\perp$ for various t_{max} values. We see that the pion v_2 increases with the amount of rescatterings, the proton v_2 decreases, while the kaon v_2 does not change significantly. This can be understood as the consequence of hadron interactions. For example, pions and protons tend to flow together at the same velocity because of their interactions. Thus, pions and protons at the same velocity (i.e., small $p_\perp$ pions and large $p_\perp$ protons) will tend to have the same anisotropy after rescatterings. This will then
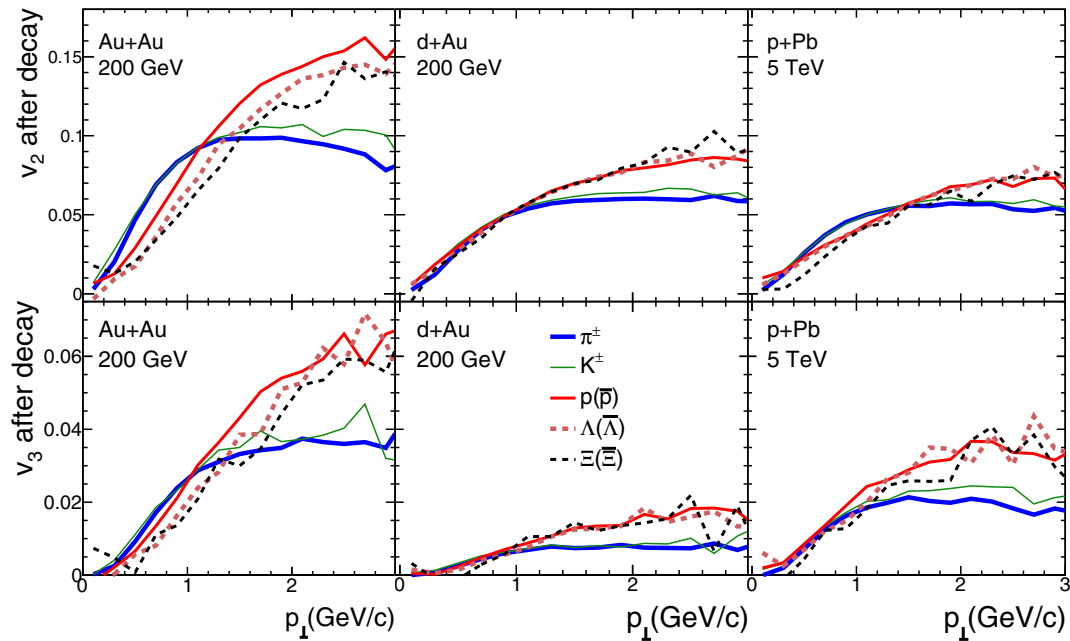

FIG. 7. Effect of decays on mass splitting. Hadron v_2 (top panels) and v_3 (bottom panels) including both primordial hadrons and decay products. Three systems are shown: $b = 6.6-8.1$ fm Au+Au collisions at $\sqrt{s_{NN}} = 200$ GeV (left column), $b = 0$ fm d+Au collisions at 200 GeV (middle column), and $b = 0$ fm p+Pb at 5 TeV (right column). Results are from string melting AMPT where hadronic rescatterings are turned off. Thick solid curves are for charged pions, thin solid curves for charged kaons, medium thick solid curves for (anti-)protons, thick dashed curves for $\Lambda(\bar{\Lambda})$, and medium thick dashed curves for $\Xi(\bar{\Xi})$.
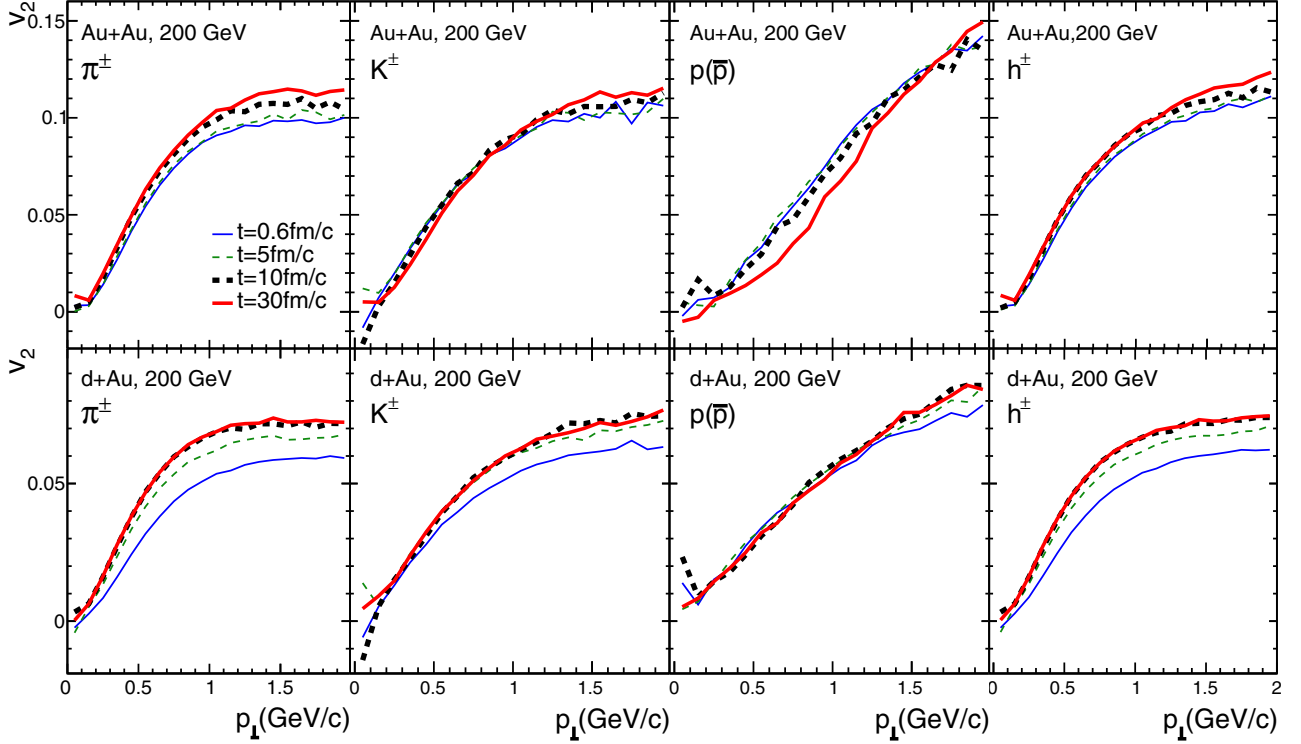
FIG. 8. Effects of hadronic rescatterings on v_2. Hadron v_2 as a function of $p_\perp$ at different stages of hadronic rescatterings in string melting AMPT. The v_2 are for final-state hadrons including resonance decays, where the final freezeout is controlled by the maximum allowed time (t_{max}) for the hadronic stage. Shown are the results for charged pions (first column), charged kaons (second column), (anti-)protons (third column), and charged hadrons (last column) in $b = 6.6-8.1$ fm Au+Au collisions at 200 GeV (top panels) and $b = 0$ fm d+Au collisions at 200 GeV (bottom panels).

lead to lower v_2 for protons and higher v_2 for pions at the same $p_\perp$ value. Similar conclusions were reached in previous hadron cascade studies [40–42] and a recent study with free-streaming evolution coupled to a hadron cascade [15].

Figure 8 also shows a small increase in the overall charged hadron v_2, and this is from the remaining finite configuration

FIG. 9. Connection to the initial hadronic eccentricity. Gain in charged hadron v_2 from hadronic rescatterings from hadronization ($t_{max} = 0.6$ fm/c) to final freezeout ($t_{max} = 30$ fm/c) as a function of the configuration space eccentricity of hadrons right after hadronization (ϵ_2^{had}) in $b = 6.6-8.1$ fm Au+Au (circles) and $b = 0$ fm d+Au (triangles) collisions at 200 GeV. The v_2 are for final-state hadrons including resonance decays.

space eccentricity before hadronic scatterings take place. In general, whether there is an overall gain in the v_2 of charged hadrons depends on the configuration geometry at the beginning of hadron cascade. Figure 8 (bottom panels) shows our results for d+Au collisions. We see that the pion v_2 increases significantly with hadronic scatterings while the proton v_2 remains roughly unchanged. Note that the overall gain in the charged hadron v_2 is larger in d+Au than Au+Au collisions, and this is from the larger eccentricity in the d+Au system at the start of hadron cascade. Therefore the changes in the pion and proton v_2 are a net effect of the mass splitting from pion-proton interactions (i.e., increase in the pion v_2 and decrease in the proton v_2) and the overall gain of v_2 for charged hadrons.

As can be seen in Fig. 8, v_2 continues to develop after hadronization in Au+Au as well as d+Au collisions. In Au+Au collisions the development happens mainly during 5–20 fm/c while in d+Au collisions the development happens earlier (mainly before 5 fm/c). The spatial anisotropy is self-quenched from the expansion and the development of momentum space anisotropy. The further increase of overall charged hadron v_2 in Fig. 8 suggests that the spatial anisotropy is not completely quenched at the time right after hadronization; a finite spatial anisotropy is present at the beginning of hadronic rescatterings which results in the further development of v_n.

We elaborate this further by examining the v_2 increase as a function of the remaining eccentricity after hadronization
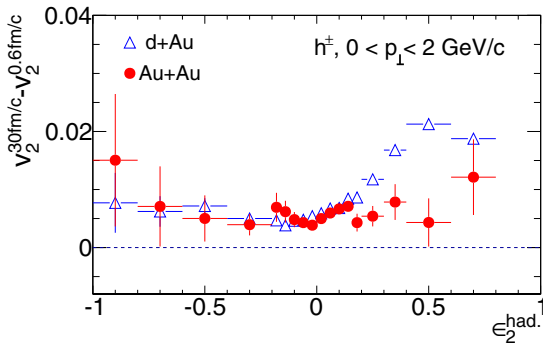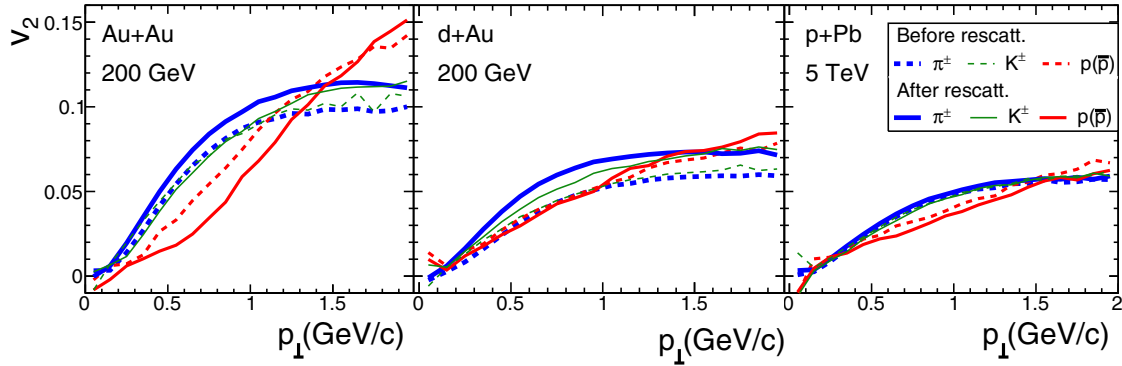
FIG. 10. Effect of hadronic rescatterings on mass splitting. Charged pions (thick curves), charged kaons (thin curves), and (anti-)proton (medium thin curves) v_2 as a function of $p_\perp$ before (dashed curves) and after (solid curves) hadron rescatterings in string melting AMPT. The effects of resonance decays are included. Three systems are shown: $b = 6.6-8.1$ fm Au+Au collisions at $\sqrt{s_{NN}} = 200$ GeV (left column), $b = 0$ fm d+Au collisions at 200 GeV (middle column), and $b = 0$ fm p+Pb at 5 TeV (right column).

(ϵ_2^{had}), i.e., the starting eccentricity for hadronic cascade. This is shown in Fig. 9 for both Au+Au and d+Au collisions. Because a typical AMPT evolution around mid-rapidity essentially ends by the time of 30 fm/c, we evaluate the increase in v_2 from hadronic scatterings as $\Delta v_2 = v_2^{30\text{fm}/c} - v_2^{0.6\text{fm}/c}$. The ϵ_2^{had} value is calculated with respect to the initial configuration space $\psi_2^{(r)}$, as is v_2. We have verified that the hadron v_2 right after the coalescence hadronization, as well as the v_2 at final freezeout, is proportional to the initial eccentricity (ϵ_2)—which is also calculated with respect to the initial $\psi_2^{(r)}$—except when ϵ_2 is large (close to one). We have also found that the ϵ_2^{had} value is positively correlated with the ϵ_2 value in Au+Au collisions, while the correlation is weak in d+Au collisions.

Figure 9 shows that, in the ϵ_2^{had} range of 0–0.2 in Au+Au and 0–0.5 in d+Au collisions, Δv_2 roughly increases linearly with ϵ_2^{had}. At large positive ϵ_2^{had}, the statistics are poor and ϵ_2^{had} may not reflect a bulk geometry any more. At negative ϵ_2^{had} events are also rare. On average, $\langle \epsilon_2^{had} \rangle$ is 0.11 in Au+Au and 0.42 in d+Au collisions, starting from an initial $\langle \epsilon_2 \rangle$ of 0.29 and 0.53 for the two collision systems, respectively. The geometric anisotropy is thus not quenched completely after partonic interactions in Au+Au collisions; the reduction in eccentricity in d+Au collisions is even smaller because of a shorter partonic stage. The remaining spatial anisotropy is smaller in Au+Au than in d+Au collisions, and this results in a smaller v_2 gain during the hadronic rescattering stage in Au+Au than in d+Au collisions, as observed in Fig. 8.
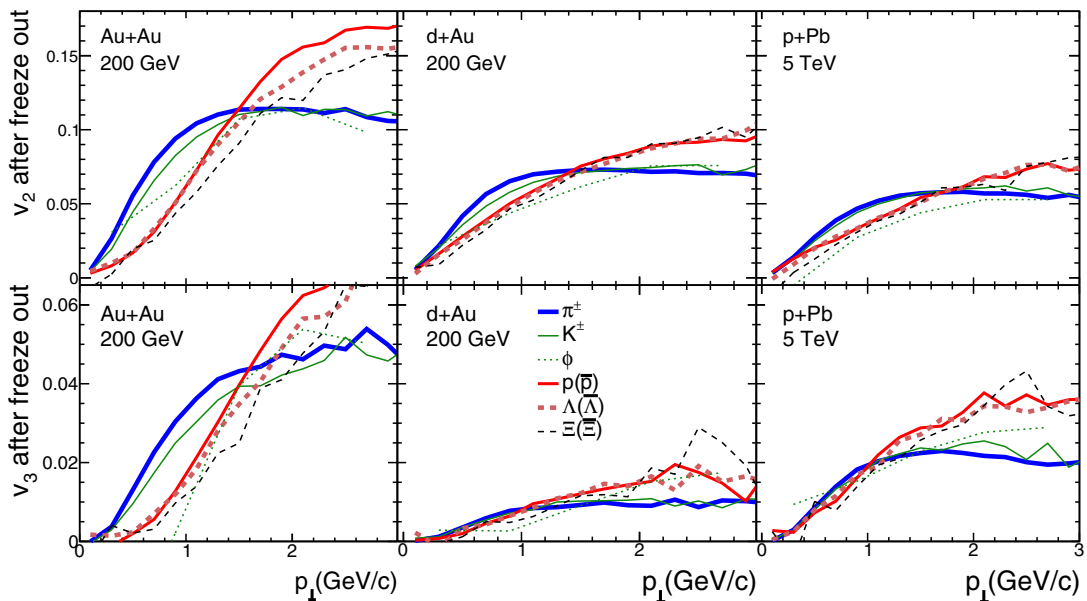

FIG. 11. Mass splitting at freezeout. Final hadron v_2 (top panels) and v_3 (bottom panels) as a function of $p_\perp$ from string melting AMPT, where resonance decays are included. Three systems are shown: $b = 6.6-8.1$ fm Au+Au collisions at $\sqrt{s_{NN}} = 200$ GeV (left column), $b = 0$ fm d+Au collisions at 200 GeV (middle column), and $b = 0$ fm p+Pb at 5 TeV (right column). Thick solid curves are for charged pions, thin solid curves for charged kaons, thin dashed curves for ϕ mesons, medium thick solid curves for (anti-)protons, thick dashed curves for $\Lambda(\bar{\Lambda})$, and medium thick dashed curves for $\Xi(\bar{\Xi})$.
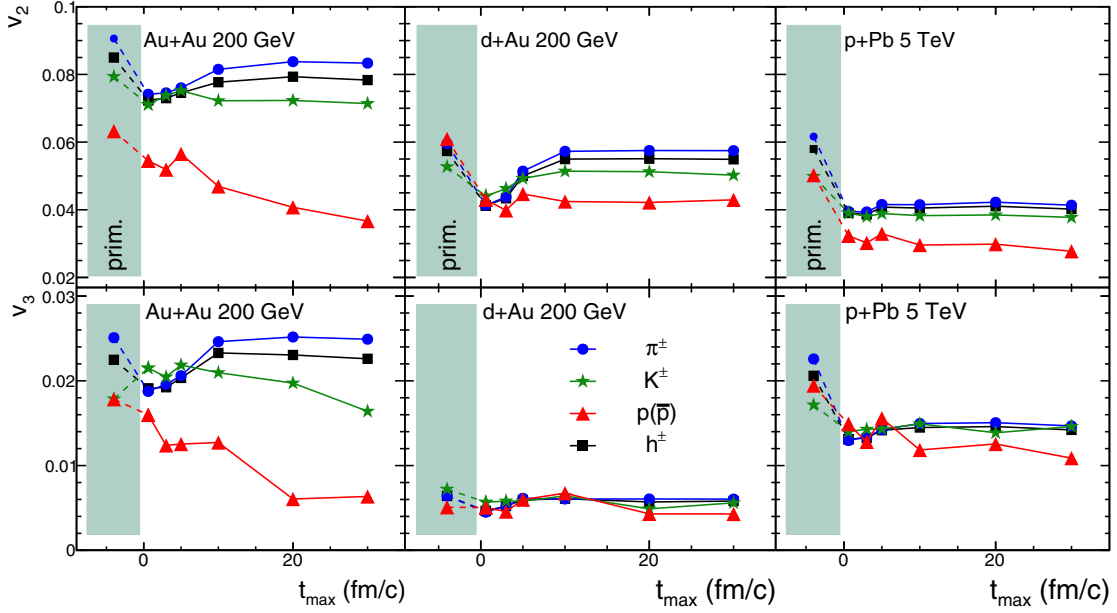
FIG. 12. Origin of v_n mass splitting. The v_2 (top panels) and v_3 (bottom panels) of charged pions, charged kaons, (anti-)protons, and charged hadrons within $0.8 < p_\perp < 1.2$ GeV/c at different stages of the collision evolution. Points plotted within the shaded areas represent primordial hadrons right after quark coalescence, points plotted at $t_{max} = 0.6$ fm/c represent results right after hadronization but including resonance decays, and points at various t_{max} values represent results after hadronic rescatterings (and resonance decays).

It is also interesting to note in Fig. 9 that Δv_2 is finite for events with $\epsilon_2^{had} = 0$, where one would naively expect $\Delta v_2 = 0$. This would indeed be true if the initial hadron $v_2^{0.6fm/c}$ (before hadronic rescatterings) was zero, analogous to the zero initial parton anisotropies $v_n^{ini} \equiv 0$ in AMPT (before partonic scatterings). However, for finite initial $v_2^{0.6fm/c} > 0$, which is the case here, it is not necessarily true that v_2 would not further develop.

Figure 10 shows hadron v_2 as a function of $p_\perp$ before hadronic rescatterings but including resonance decays in dashed curves and v_2 of freezeout hadrons after hadronic rescatterings in solid curves. As shown, hadronic rescatterings make significant contributions to the mass splitting in the final-state hadron v_2. Meanwhile the absolute gain of the v_2 magnitude is relatively small during the hadronic stage.

VII. DISCUSSIONS

Figure 11 shows v_2 and v_3 of final-state hadrons as a function of $p_\perp$ in Au+Au and d+Au collisions at 200 GeV and p+Pb collisions at 5 TeV. The ϕ mesons are all decayed in the final state of AMPT, so they are reconstructed by the invariant mass of K^+K^- pairs [43] and $K_S K_L$ pairs with combinatorial background subtraction, as usually done in experiments [44]. The mass splitting of v_n at low $p_\perp$ is more obvious in Au+Au collisions than small systems. There is also splitting in v_n at high $p_\perp$, likely more from the number of constituent quarks rather than the mass difference.

We summarize our results on the mass splitting of v_2 with Fig. 12, which shows the v_2 of pions, kaons, protons, and antiprotons, and charged hadrons within a fixed $p_\perp$ bin of $0.8 < p_\perp < 1.2$ GeV/c, as an example. Different stages of

the collision system evolution are shown: (i) right after the quark coalescence hadronization including only primordial particles (data points plotted to the left of $t_{max} = 0$); (ii) right after the quark coalescence but including resonance decays (data points plotted at $t_{max} = 0.6$ fm/c); (iii) after various degrees of hadronic rescatterings, which are obtained from freezeout particles by setting t_{max} to the corresponding values as plotted. As shown in Fig. 12, most of the overall v_n is built up in the partonic phase, while the additional gain in the overall v_n from hadronic rescatterings is small. On the other hand, although there is often a significant mass splitting in the primordial hadron v_n right after hadronization from the kinematics in the quark coalescence process, the mass splitting is often reduced when decay products are included in v_n. In other words, the mass splitting before hadronic rescatterings is usually small. This small mass splitting does not change significantly during the first 5 fm/c in Au+Au collisions, because the partonic stage dominates the early evolution. We also see that a significant mass splitting is built up during the time of 5–20 fm/c of hadronic rescatterings. After 20 fm/c there is little further change in the v_n in d+Au or p+Pb collisions, while in Au+Au there is still a small increase in the size of mass splitting.

VIII. CONCLUSIONS

We have studied the developments of the mass splitting of hadron v_n at different stages of nuclear collisions with a multiphase transport model AMPT. First results on Au+Au and d+Au collisions at the top RHIC energy were published in Ref. [30]. The present work provides extensive details to that earlier study by including more hadron species such as

resonances and strange hadrons. We also expand the investigation to the triangular flow v_3 and p+Pb collisions at the LHC energy of 5 TeV. We reach the same conclusion for v_2 and v_3, for both heavy ion collisions and small-system collisions, in that the mass splitting of hadron v_n is partly from the quark coalescence hadronization process but more importantly from hadronic rescatterings. Although the overall v_n amplitude is dominantly developed during the partonic stage, the mass splitting is usually small right after hadronization, especially after including resonance decays. The majority of the hadron mass splitting is developed in the hadronic rescattering stage, even though the gain in the overall v_n of charged particles is small there. These qualitative conclusions are the same as those from hybrid models that couple hydrodynamics to a hadron cascade, even though in transport models such as AMPT the anisotropic parton escape is the major source of v_n. In the ϕ-randomized test of AMPT, where the anisotropic parton escape is the only source of v_n, we also observe similar mass splitting of hadron v_n. Therefore we conclude that the mass splitting of v_n can be an interplay of several physics processes and is not a unique signature of hydrodynamic collective flow.

[1] I. Arsene *et al.*, Quark gluon plasma and color glass condensate at RHIC? The Perspective from the BRAHMS experiment, Nucl. Phys. A **757**, 1 (2005).

[2] B. B. Back *et al.*, The PHOBOS perspective on discoveries at RHIC, Nucl. Phys. A **757**, 28 (2005).

[3] J. Adams *et al.*, Experimental and theoretical challenges in the search for the quark gluon plasma: The STAR Collaboration's critical assessment of the evidence from RHIC collisions, Nucl. Phys. A **757**, 102 (2005).

[4] K. Adcox *et al.*, Formation of dense partonic matter in relativistic nucleus-nucleus collisions at RHIC: Experimental evaluation by the PHENIX collaboration, Nucl. Phys. A **757**, 184 (2005).

[5] B. Muller, J. Schukraft, and B. Wyslouch, First Results from Pb+Pb collisions at the LHC, Ann. Rev. Nucl. Part. Sci. **62**, 361 (2012).

[6] U. Heinz and R. Snellings, Collective flow and viscosity in relativistic heavy-ion collisions, Ann. Rev. Nucl. Part. Sci. **63**, 123 (2013).

[7] C. Gale, S. Jeon, and B. Schenke, Hydrodynamic modeling of heavy-ion collisions, Int. J. Mod. Phys. A **28**, 1340011 (2013).

[8] B. I. Abelev *et al.*, Systematic measurements of identified particle spectra in pp,d^+ Au and Au+Au collisions from STAR, Phys. Rev. C **79**, 034909 (2009).

[9] J.-Y. Ollitrault, Anisotropy as a signature of transverse collective flow, Phys. Rev. D **46**, 229 (1992).

[10] R. Andrade, F. Grassi, Yogiro Hama, T. Kodama, and O. Socolowski Jr., On the Necessity to Include Event-By-Event Fluctuations in Experimental Evaluation of Elliptical Flow, Phys. Rev. Lett. **97**, 202302 (2006).

[11] B. Alver and G. Roland, Collision geometry fluctuations and triangular flow in heavy-ion collisions, Phys. Rev. C **81**, 054905 (2010); **82**, 039903(E) (2010).

[12] F. Cooper and G. Frye, Comment on the single particle distribution in the hydrodynamic and statistical thermodynamic models of multiparticle production, Phys. Rev. D **10**, 186 (1974).

[13] T. Hirano, U. W. Heinz, D. Kharzeev, R. Lacey, and Y. Nara, Mass ordering of differential elliptic flow and its violation for phi mesons, Phys. Rev. C **77**, 044909 (2008).

[14] H. Song, S. A. Bass, and U. Heinz, Viscous QCD matter in a hybrid hydrodynamic+Boltzmann approach, Phys. Rev. C **83**, 024912 (2011).

[15] P. Romatschke, Collective flow without hydrodynamics: simulation results for relativistic ion collisions, Eur. Phys. J. C **75**, 429 (2015).

[16] Z.-W. Lin and C. M. Ko, Partonic effects on the elliptic flow at RHIC, Phys. Rev. C **65**, 034904 (2002).

[17] Z.-W. Lin, C. M. Ko, B.-A. Li, B. Zhang, and S. Pal, A multiphase transport model for relativistic heavy ion collisions, Phys. Rev. C **72**, 064901 (2005).

[18] Z.-W. Lin, Evolution of transverse flow and effective temperatures in the parton phase from a multiphase transport model, Phys. Rev. C **90**, 014904 (2014).

[19] A. Adare *et al.*, Measurement of Long-Range Angular Correlation and Quadrupole Anisotropy of Pions and (Anti)Protons in Central d + Au collisions at $\sqrt{s_{NN}} = 200$ GeV, Phys. Rev. Lett. **114**, 192301 (2015).

[20] L. Adamczyk *et al.*, Long-range pseudorapidity dihadron correlations in d+Au collisions at $\sqrt{s_{NN}} = 200$ GeV, Phys. Lett. B **747**, 265 (2015).

[21] V. Khachatryan *et al.*, Observation of long-range near-side angular correlations in proton-proton collisions at the LHC, J. High Energy Phys. 09 (2010) 091.

[22] S. Chatrchyan *et al.*, Observation of long-range near-side angular correlations in proton-lead collisions at the LHC, Phys. Lett. B **718**, 795 (2013).

[23] B. Abelev *et al.*, Long-range angular correlations on the near and away side in p-Pb collisions at $\sqrt{s_{NN}} = (5).02$ TeV, Phys. Lett. B **719**, 29 (2013).

[24] G. Aad *et al.*, Observation of Associated Near-side and Away-side Long-range Correlations in $\sqrt{s_{NN}} = (5).02$ TeV Proton-lead Collisions with the ATLAS Detector, Phys. Rev. Lett. **110**, 182302 (2013).

[25] P. Bozek, Elliptic flow in proton-proton collisions at $\sqrt{(S)} = 7$ TeV, Eur. Phys. J. C **71**, 1530 (2011).

[26] P. Bozek and W. Broniowski, Correlations from hydrodynamic flow in p-Pb collisions, Phys. Lett. B **718**, 1557 (2013).

[27] A. Bzdak and G.-L. Ma, Elliptic and Triangular Flow In p+Pb and Peripheral Pb+Pb Collisions from Parton Scatterings, Phys. Rev. Lett. **113**, 252301 (2014).

[28] L. He, T. Edmonds, Z.-W. Lin, F. Liu, D. Molnar, and F. Wang, Anisotropic parton escape is the dominant source of azimuthal anisotropy in transport models, Phys. Lett. B **753**, 506 (2016).

[29] Z.-W. Lin, L. He, T. Edmonds, F. Liu, D. Molnar, and F. Wang, Elliptic anisotropy v_2 may be dominated by particle escape instead of hydrodynamic flow, Nucl. Phys. A **956**, 316 (2016).

[30] H. Li, L. He, Z.-W. Lin, D. Molnar, F. Wang, and W. Xie, Origin of the mass splitting of elliptic anisotropy in a multiphase transport model, Phys. Rev. C **93**, 051901 (2016).

[31] AMPT source files are available online at http://myweb.ecu.edu/linz/ampt/.

[32] B. Zhang, ZPC 1.0.1: A Parton cascade for ultrarelativistic heavy ion collisions, Comput. Phys. Commun. **109**, 193 (1998).

[33] Y. Oh, Z.-W. Lin, and Che Ming Ko, Deuteron production and elliptic flow in relativistic heavy ion collisions, Phys. Rev. C **80**, 064902 (2009).

[34] J.-Y. Ollitrault, Determination of the reaction plane in ultrarelativistic nuclear collisions, Phys. Rev. D **48**, 1132 (1993).

[35] S. Voloshin and Y. Zhang, Flow study in relativistic nuclear collisions by Fourier expansion of Azimuthal particle distributions, Z. Phys. C **70**, 665 (1996).

[36] Z.-W. Lin, Quark coalescence with quark number conservation and the effect on quark-hadron scaling, J. Phys. G **38**, 075002 (2011).

[37] G. Eyyubova, L. V. Bravina, E. Zabrodin, V. L. Korotkikh, I. P. Lokhtin, L. V. Malinina, S. V. Petrushanko, and A. M. Snigirev, Jets and decays of resonances: Two mechanisms responsible for reduction of elliptic flow at the CERN Large Hadron Collider (LHC) and restoration of constituent quark scaling, Phys. Rev. C **80**, 064907 (2009).

[38] Z. Qiu, C. Shen, and U. W. Heinz, Resonance decay contributions to higher-order anisotropic flow coefficients, Phys. Rev. C **86**, 064906 (2012).

[39] J. Crkovská *et al.*, Influence of jets and final-state interactions on the triangular flow in ultrarelativistic heavy-ion collisions, Phys. Rev. C **95**, 014910 (2017).

[40] G. Burau, J. Bleibel, C. Fuchs, Amand Faessler, L. V. Bravina, and E. E. Zabrodin, Anisotropic flow of charged and identified hadrons in the quark-gluon string model for Au + Au collisions at $\sqrt{s_{NN}} = 200$ GeV, Phys. Rev. C **71**, 054905 (2005).

[41] H. Petersen, Q. Li, X. Zhu, and M. Bleicher, Directed and elliptic flow in heavy ion collisions at GSI-FAIR and CERN-SPS, Phys. Rev. C **74**, 064908 (2006).

[42] Y. Zhou, X. Zhu, P. Li, and H. Song, Investigation of possible hadronic flow in $\sqrt{s_{NN}} = 5.02$ TeV $p - Pb$ collisions, Phys. Rev. C **91**, 064908 (2015).

[43] S. Pal, C. M. Ko, and Z.-W. Lin, Phi meson production in relativistic heavy ion collisions, Nucl. Phys. A **707**, 525 (2002).

[44] B. I. Abelev *et al.*, Measurements of phi meson production in relativistic heavy-ion collisions at RHIC, Phys. Rev. C **79**, 064903 (2009).